

Supporting Information

High-rate in-plane micro-supercapacitors scribed onto photo paper using in-situ femtolaser-reduced graphene oxide/Au nanoparticle microelectrodes

Ruo-Zhou Li, Rui Peng, Kenneth D. Kihm, Shi Bai, Denzel Bridges, Uma Tumuluri, Zili Wu, Tong Zhang*, Giuseppe Compagnini, Zhili Feng and Anming Hu*

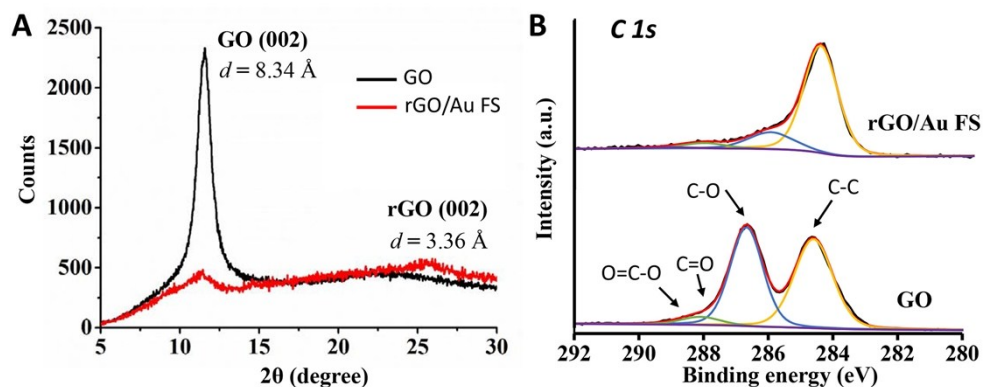


Fig. S1. A) XRD patterns of GO (black) and rGO/Au FS microelectrodes (red). D-spacing of GO (before the laser scan) and rGO sheets in rGO/Au microelectrodes (after the laser scan) are marked near the GO (002) and rGO (002) peaks, confirming the reduction of GO, and B) X-ray photoelectron spectra (XPS)-fitted C 1s core peaks for GO and rGO/Au FS microelectrodes, showing the removal of oxygen-containing functional groups. The average laser power is 80 mW.

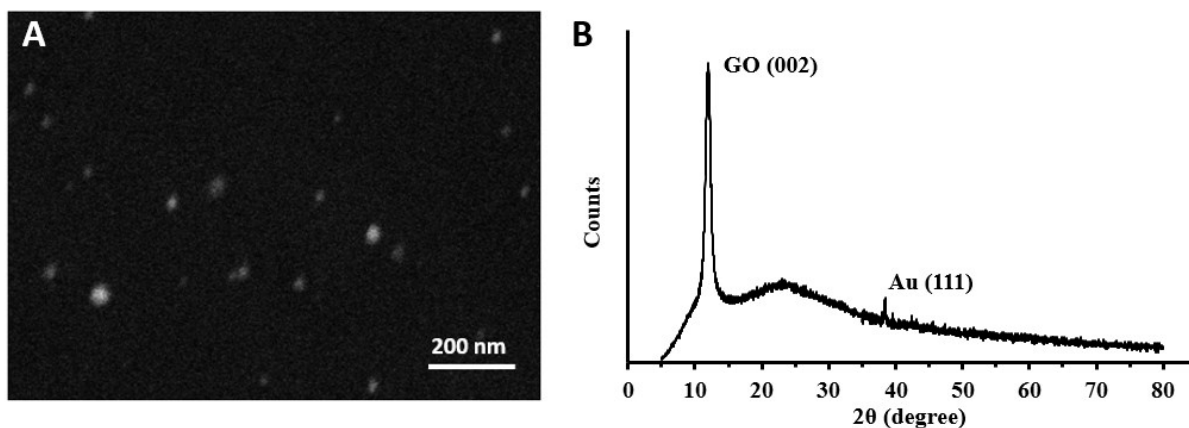


Fig. S2. A) SEM image and B) XRD pattern showing that a few Au nanoparticles can be formed on GO surface. The average diameter of Au NPs is less than 20 nm.

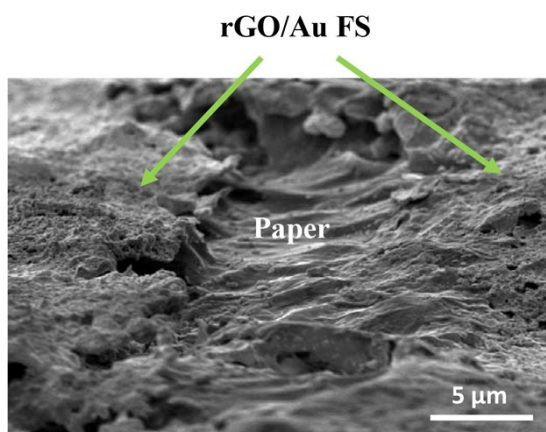


Fig. S3. SEM image of a damaged area of femtolaser-written rGO/Au FS microelectrode at a laser power of 200 mW. The section of rGO/Au film was entirely removed to be exposed of the cellulose fibers of paper substrate.

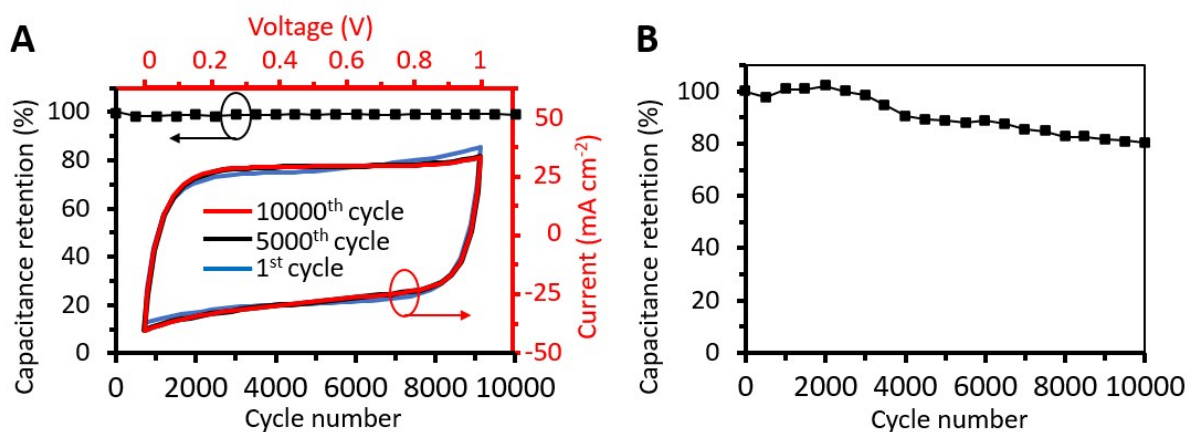


Fig. S4. A) The capacitance retention for the cycle numbers up to 10,000 and corresponding CV curves measured at 50 V·s⁻¹, and B) the capacitance retention for the cycle numbers up to 10,000 at 1 V·s⁻¹.

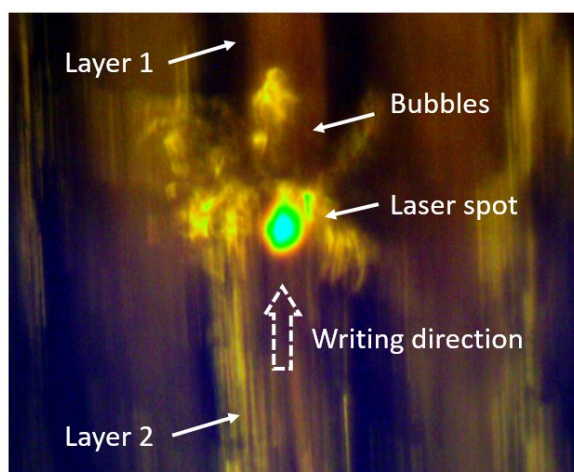


Fig. S5. The optical image captured from an optical microscope shows bubble generation during laser writing of the second layer; the dotted white arrow delineates the writing direction.

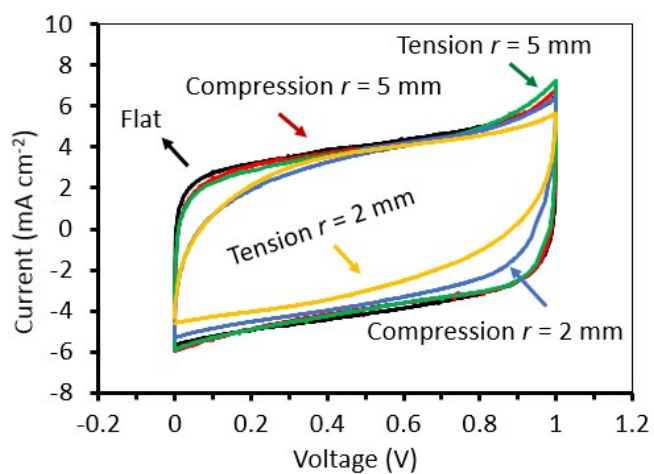


Fig. S6. Comparative CV curves of a 3D rGO/Au FS-MSC (5-layer) under compression or tension-bending conditions at a scanning rate of $1 \text{ V}\cdot\text{s}^{-1}$.

Supplementary Note 1:

Calculation of specific capacitance for MSCs

The capacitance of a MSC C was calculated from the CV data according to the following equation:

$$C = \frac{1}{v(V_f - V_i)} \int_{V_i}^{V_f} I(V) dV \quad (1)$$

where v is the scan rate, V_f and V_i are the integration potential limits of the CV curves and

$I(V)$ is the **discharge** current as a function of voltage. The areal capacitance $C_{area} = \frac{C}{A}$ was

calculated by taking the whole surface area A of the MSCs into account, including the microelectrode surface and the interspaces between them. The stack capacitances

$C_{stack} = \frac{C}{V}$ were calculated based on the volume of micro electrodes and the interspaces

between the electrodes. The thickness of each component of the device was measured through SEM.

Supplementary Note 2:

Comparison of reduction mechanisms by FS laser and CW laser

The photonic reduction of GO/HAuCl₄ is attributed to the absorption of laser energy¹ in either a single- or multi-photon process. Threshold laser power of 44 mW was observed for both the FS laser and CW laser at a scan rate of 1 mm S⁻¹. No apparent reduction was observed at a laser power below threshold. The reduction mechanism for FS laser can be described in two stages: 1) multi-photon reduction when the laser power right above the threshold, and 2) single-photon thermal reduction, sintering and melting at a higher laser power (for example, 80 mW and 200 mW). In contrast, CW laser irradiation only leads to a single-photon reduction and photothermal sintering with increasing laser power.

At a laser power right above the threshold, the multi-photon reduction of GO/HAuCl₄ by FS laser is evidenced by the UV-NIR absorption spectra as shown in Fig. S7. There is no remarkable absorption band at 1030 nm (absorption is less than 3%) corresponding to the FS laser, whereas the absorption at 515 nm (the double frequency of FS laser), which implies a double-photon absorption, is 12.3%, approximate to that of 10.8% at 532 nm corresponding to the CW laser. Since the measured threshold power is at a similar value for both 1030 nm and 532 nm, a double-photon absorption should occur in focused femtolaser at 1030 nm.

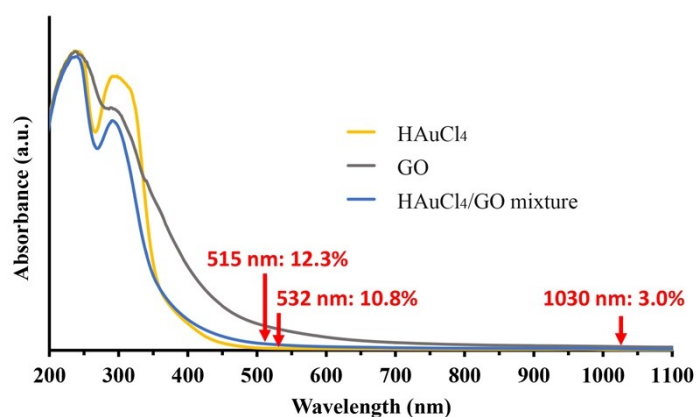


Fig. S7. UV-Vis absorption spectra of H₂AuCl₄, GO, and H₂AuCl₄/GO mixture. The absorption levels for the femtolaser (1030 nm for single-photon and 515 nm for double-photons) and of the CW laser (532 nm) are marked in red numbers.

Further evidence is given by the laser line absorption of GO/H₂AuCl₄ composite membrane measured by an ultrasensitive fiber laser power meter at a much lower laser power than the reduced threshold. Essentially, the multi-photon absorption (FS laser) shows non-linear absorption behaviors, whereas the single-photon absorption (CW laser) shows linear absorption behaviors. For example, through a two-photon process the absorbed power is proportional to the square of the input power, while in a single-photon process the absorbed power is directly proportional to the input power.² At a laser power (1 mW) well below the threshold, the absorbed power of unfocused FS laser is less than 70% of the absorbed CW laser power. Nevertheless, both the FS and CW lasers share the similar threshold laser power as aforementioned. Therefore, the two-photon or a higher-photon process must take a dominant role for FS laser reduction at a laser power right above the threshold compared with CW laser reduction.

With increasing laser power (for example, 80 mW and 200 mW), an enhanced photothermal effect is generated, which increases the temperature at the vicinity of the focal point.^{3, 4} This can be attributed to the strong absorption of produced Au NPs attached on rGO surface through surface plasmon resonance.^{3, 4} For the FS laser, at a laser power of 80 mW, the photothermal effect promotes reduction of GO/H₂AuCl₄ and sintering (i.e. solid state diffusion) of Au NPs. Upon further increasing the laser power to 200 mW, the photothermal effect takes a significant role with a strong heat accumulation, resulting in the coalescence of Au nanoparticles and the formation of Au spheres.⁵ For the CW laser, in principal, at the same laser power, a single-photon process generates a stronger photothermal effect than a multi-photon process by FS laser. Thus, the sintering and

possible melting of Au NPs occur at a low laser power (for example, 50 mW) for the CW laser than the laser power of the FS laser, which is consistent with the XRD results as shown in Fig.

S8.

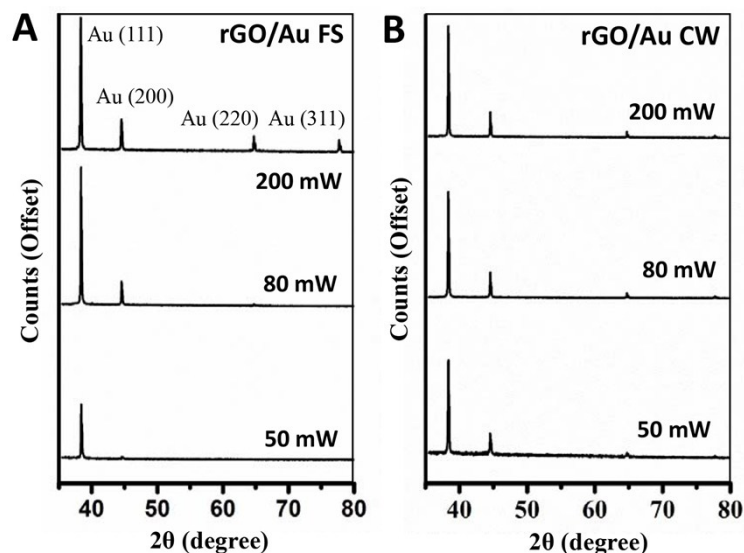


Fig. S8. X-ray diffraction (XRD) patterns of A) the rGO/Au FS microelectrode and B) the rGO/Au CW microelectrode under the laser powers of 50 mW, 80 mW and 200 mW. The rGO/Au FS microelectrode shows a significant increase of the ratio of (200) peak to (111) peak with increasing laser power, which is consistent with the morphology changes from monodispersed Au NPs (50 mW) to sintered Au network (80 mW), and then to Au microspheres (200 mW). In contrast, for the rGO/Au CW microelectrode, the (200) peak to (111) peak ratio shows minor increase with increasing laser power, which is also consistent with that the significant sintering of Au NPs occurs at lower laser power (50 mW) for the case of CW laser.

Supplementary Note 3:

Femtolaser-enhanced reduction of GO sheets of rGO/Au FS microelectrode.

The enhanced reduction of GO sheets is observed in rGO/Au FS microelectrode as the X-ray photoelectron spectra (XPS) shown in Fig. S9 with the highest molecular proportion ratio of C to O, $C/O = 12.53$ at a laser power of 80 mW (Table S1). This C/O ratio is higher than those reported laser-reduced graphene oxide⁶ and comparable with those chemical and plasmon reduced graphene oxides⁷ for MSCs. The high C/O ratio can be attributed to addition of Au, FS laser reduction and enhanced reduction with increase of laser power as shown in Table S1.

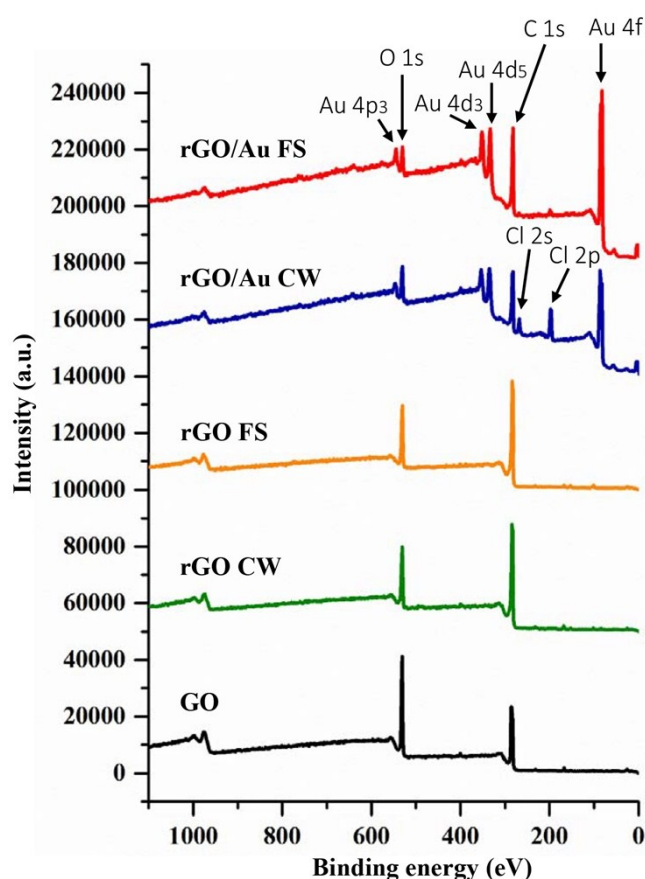


Fig. S9. X-ray Photoelectron Spectroscopy (XPS) surveys of GO, rGO CW, rGO FS, rGO/Au CW, and rGO/Au FS, showing a more pronounced reduction of GO and Au ions by the FS laser than by the CW laser. The average laser power of both lasers was kept constant 80 mW.

Table S1. Atomic concentrations and C/O ratios of GO, rGO FS, rGO/Au FS, rGO CW, and rGO/Au CW.

Laser type	FS laser					CW laser			
Material	GO	rGO		rGO/Au		rGO		rGO/Au	
Power [mW]		50	80	50	80	50	80	50	80
C 1s	65.7	67.2	79.6	73.6	81.7	70.1	78	69.9	69
O 1s	31.5	29.9	18.7	8.8	6.5	27.6	19.2	16.6	14.9
Au 4f	0	0	0	7.1	6.9	0	0	2.7	6.4
Cl 2p	0	0	0	7.6	1.9	0	0	7.1	9.4
C/O	2.09	2.24	4.26	8.37	12.57	2.54	4.06	4.21	4.63

Supplementary Note 4:

Mechanical flexibility of rGO/Au FS MSCs.

By far, most MSCs are fabricated on stiff substrates-with limited abilities to sustain mechanical deformations such as bending, whereas flexible electronics have attracted increasing attention recently. The flexibility offers the possibility of conforming the devices to curved surfaces and also enables large scale roll-to-roll manufacturing.⁸ Combined with the flexibility of the gel electrolyte and paper substrate, the fabricated MSCs could maintain their capacitive functionality when subjected to mechanical bending.⁹ The bending test conducted at a bending radius larger than 5 mm, shows minimized change in electrode resistance (Fig. S10A). The slight increase of electrode resistance for tension is mainly due to the elongated conductive path way after bending. As a result, no obvious change is observed at the CV curves of rGO/Au FS MSC for compression (Fig. S10B), which is comparable to that of previously reported flexible MSCs.

At a very small bending radius such as 2 mm, bending of the rGO/Au FS microelectrode can alter its resistivity differently for compression and for tension (Fig. S10A). The resistivity/conductivity of rGO/Au FS is determined primarily by sintered Au NPs that are closely congregated (Fig. 2B). When compressed, the electron pathways between the sintered Au-NPs will become slightly shorter as the compression energy is also consumed to laterally deform the rGO/Au FS sheet. This results in little or no resistivity reduction as the bending radius decreases.^{10, 11} In contrast, under tension the electron pathways are more significantly extended and the areal densities of Au NPs are decreased, occasionally disrupting the electron pathways between them.^{11, 12} The resulting resistivity increases continually with decreasing bending radius. Under compression, the capacitance, measured

at $1 \text{ V}\cdot\text{s}^{-1}$, remains unchanged when the bending radius changes from 5 mm to 2 mm (Fig. S10B). However, under tension the capacitance moderately decreases with the same corresponding change in bending radius. This is consistent with the more pronounced increase of the resistivity for tension, in contrast to no observed notable changes of the resistivity for the case of compression. This asymmetric bending behavior occurred at a small bending radius, further implying the role of electrode resistance in the MSC performance. In general, this proposed paper-based MSCs can be subjected to mechanical bending at a bending radius larger than 5 mm, while the compressive deformation is preferable for smaller bending radii.

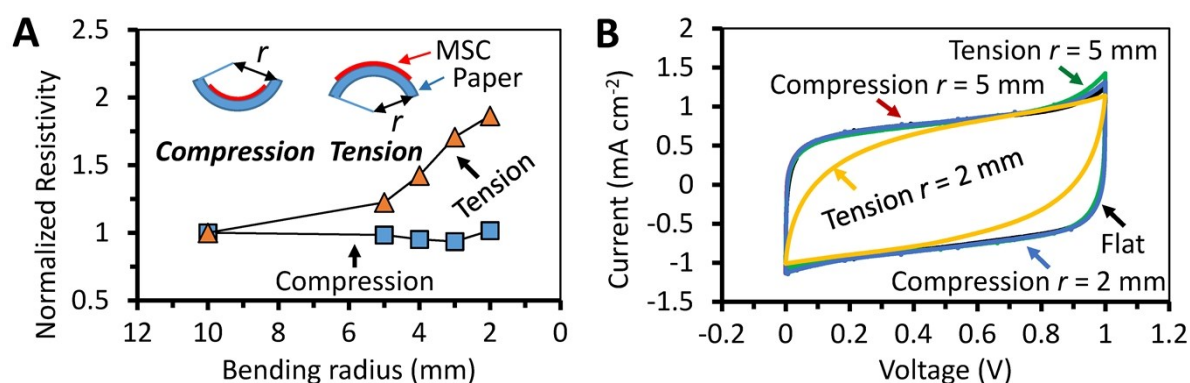


Fig. S10. A) The resistivity of rGO/Au FS-MSC as functions of the bending radius for both cases of compression and tension, B) comparative CV curves of the rGO/Au FS-MSC under the opposite bending conditions at $1 \text{ V}\cdot\text{s}^{-1}$.

Supplementary Note 5:

Electrochemistry performance of rGO/Au MSCs with different concentrations of HAuCl_4

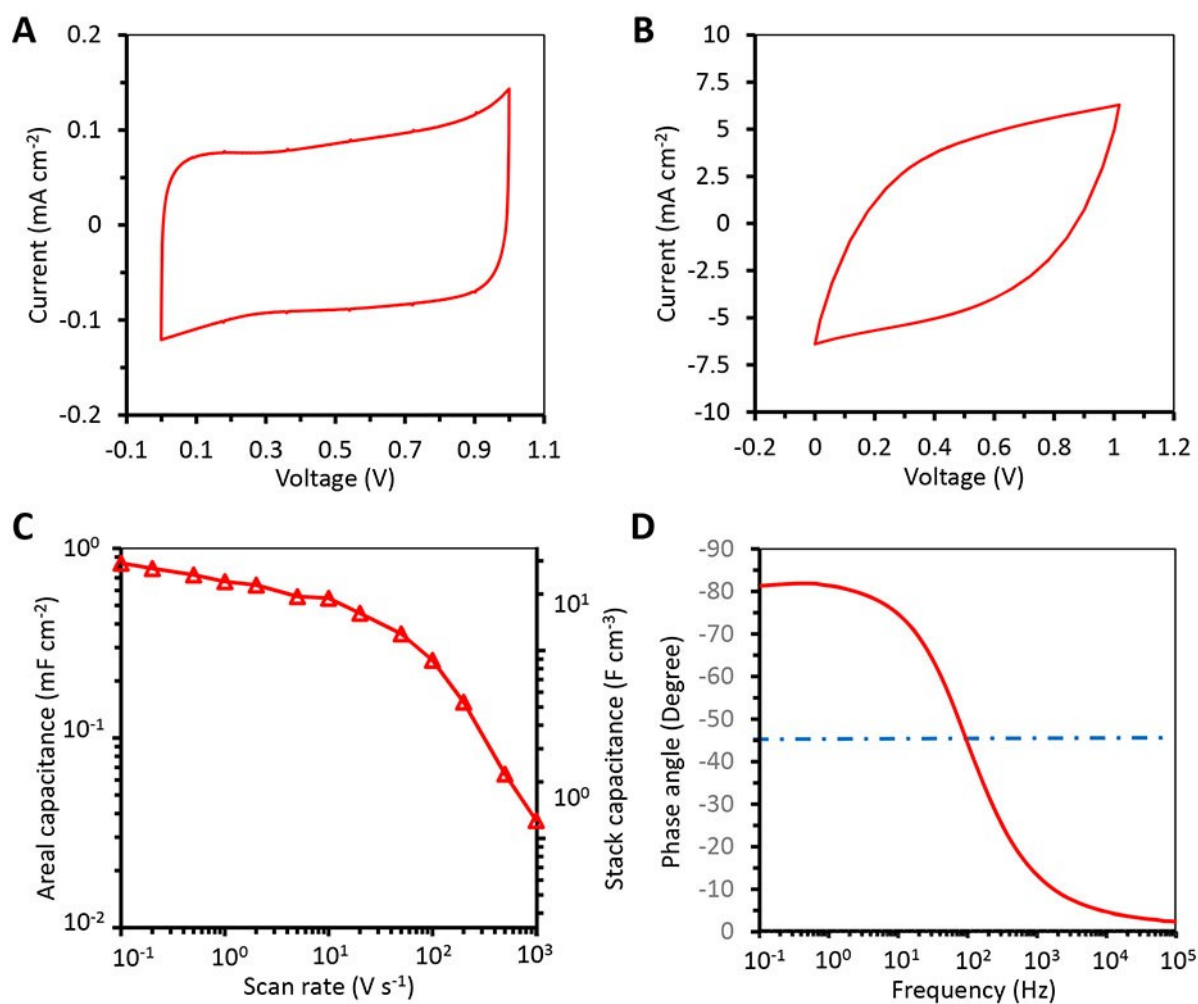


Fig. S11. Electrochemical performances of the laser-written rGO/Au-MSCs with a HAuCl_4 concentration of 0.25 M in $7.5 \text{ mg}\cdot\text{mL}^{-1}$ GO suspension: A), B) cyclic voltammetry (CV) curves obtained at a scan rate of $1 \text{ V}\cdot\text{s}^{-1}$ and $100 \text{ V}\cdot\text{s}^{-1}$, respectively, C) areal capacitance and stack capacitance as a function of the scan rate, D) the Bode plot of impedance of the MSC.

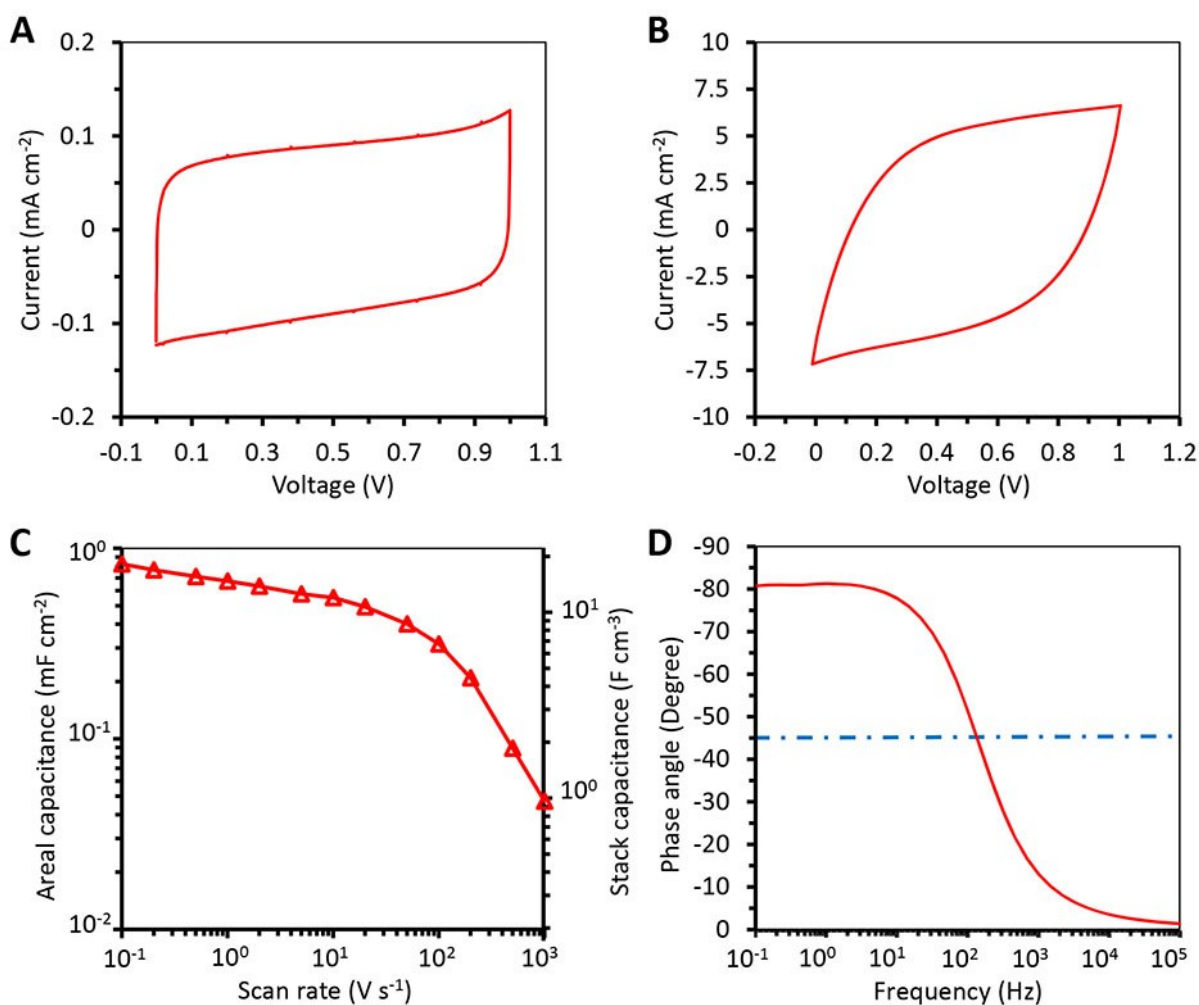


Fig. S12. Electrochemical performances of the laser-written rGO/Au-MSCs with a HAuCl_4 concentration of 0.5 M in $7.5 \text{ mg}\cdot\text{mL}^{-1}$ GO suspension: A, B) cyclic voltammetry (CV) curves obtained at a scan rate of $1 \text{ V}\cdot\text{s}^{-1}$ and $100 \text{ V}\cdot\text{s}^{-1}$, respectively, C) areal capacitance and stack capacitance as a function of the scan rate, D) the Bode plot of impedance of the MSC.

References

1. S. Shukla, X. Vidal, E. P. Furlani, M. T. Swihart, K.-T. Kim, Y.-K. Yoon, A. Urbas and P. N. Prasad, *Acs Nano*, 2011, **5**, 1947-1957.
2. C. Zheng, A. Hu, K. D. Kihm, Q. Ma, R. Li, T. Chen and W. Duley, *Small*, 2015, **11**, 3006-3006.
3. A. F. Zedan, S. Moussa, J. Turner, G. Atkinson and M. S. El-Shall, *ACS nano*, 2012, **7**, 627-636.

4. D. K. Lim, A. Barhoumi, R. G. Wylie, G. Reznor, R. S. Langer and D. S. Kohane, *Nano Lett*, 2013, **13**, 4075-4079.
5. D. Liu, C. Li, F. Zhou, T. Zhang, H. Zhang, X. Li, G. Duan, W. Cai and Y. Li, *Scientific reports*, 2015, **5**, 7686.
6. W. Gao, N. Singh, L. Song, Z. Liu, A. L. Reddy, L. Ci, R. Vajtai, Q. Zhang, B. Wei and P. M. Ajayan, *Nature nanotechnology*, 2011, **6**, 496-500.
7. Z. S. Wu, K. Parvez, X. Feng and K. Mullen, *Nature communications*, 2013, **4**, 2487.
8. X. Lu, M. Yu, G. Wang, Y. Tong and Y. Li, *Energy & Environmental Science*, 2014, **7**, 2160-2181.
9. G. Lee, D. Kim, D. Kim, S. Oh, J. Yun, J. Kim, S.-S. Lee and J. S. Ha, *Energy & Environmental Science*, 2015, **8**, 1764-1774.
10. Y. Tang, S. Gong, Y. Chen, L. W. Yap and W. Cheng, *ACS nano*, 2014, **8**, 5707-5714.
11. C. F. Guo, T. Sun, Q. Liu, Z. Suo and Z. Ren, *Nature communications*, 2014, **5**, 3121.
12. P. Lee, J. Lee, H. Lee, J. Yeo, S. Hong, K. H. Nam, D. Lee, S. S. Lee and S. H. Ko, *Adv Mater*, 2012, **24**, 3326-3332.